JOURNAL OF MATERIALS SCIENCE 26 (1991) 2397–2409

Structural evaluation of phosphate bonded ceramic composite materials from non-destructive ultrasonic velocity and attenuation measurements

B. BRIDGE*, R. ROUND‡, A. GREEN§
Department of Electrical and Electronic Engineering, South Bank Polytechnic, 103 Borough Road, London SE1 0AA, UK

The fabrication of a ceramic consisting of a matrix of newberyite and aluminium orthophospate filled with alumina and lesser amounts of carbon and glass fibre, is described. This material, whilst combining excellent insulation properties with forgiving fracture, is easy to produce by moulding without sintering. The ceramic has been characterized by a number of complementary ultrasonic techniques in the frequency range 24 kHz to 5 MHz.

Dynamic elastic moduli measurements have been found to agree well with elastic constants calculated theoretically by treating the matrix and filler as end members of a two-phase material whose properties obey the lower Hashin and Shtrikman bound. In addition the bulk modulus of the matrix computed theoretically from crystallographic data and making an allowance for porosity agreed closely with the experimental modulus. Thus ultrasound velocity (moduli) measurements combined with theory can be used for non-destructive monitoring and quality control of the ceramic composition which is subject to variation with the parameters governing the chemical reaction during preparation. The theoretical bulk modulus of the ideal (pore-free) matrix is 10.4 GPa. This matrix modulus is far less than that of the moduli of the constituent oxides in the starting mixture. The reason for this is the large expansion in the sizes of closed rings of cation–oxygen network bonds that takes place in the reaction, rather than structural weakening (breaking of rings of network bonds) by hydration.

The frequency dependence of ultrasonic attenuation has been used to identify scattering regimes and thus determine the dimensions of the major scattering particles. Grain sizes determined ultrasonically for the three compositions showed excellent agreement with values determined by optical microscopy.

The high frequency dependent absorption and scattering in this material, mean that good ultrasound propagation is obtained only at low frequencies. The lowest frequency at which the ultrasonic propagation and properties are dependent on the material structure alone, i.e. independent of sample size, has been established to be 2 MHz with conveniently sized test pieces of dimensions 1.5 × 1.5 × 6 cm^3.

1. Introduction

When Al_2O_3 and MgO powders react chemically with a solution of $Al(H_2PO_4)_3$, a multiphase ceramic, consisting of several polycrystalline magnesium and aluminium phosphates with water of crystallization in specific crystalline planes, is produced. This material which is almost as easy to mould as a polymer, and needs no sintering, has excellent refractoriness and thermal and electrical insulation properties. Carbon or glass fibres can be incorporated to impart stiffness, fracture toughness and forgiving fracture.

For many years similar ceramic materials have been used for refractory lining bricks and gunned furnace repairs. Dental ceramics have also been based on these reactions. By virtue of its unusual combination of thermal and mechanical properties this ceramic has been envisaged, amongst other uses, for stealth technology applications, e.g. the minimization of infrared

* *Previous address*: Department of Physics, Brunel University, Kingston Lane, Uxbridge, Middlesex, UK.
‡ *Previous address*: Department of Physics, Brunel University. Now at the Department of Ceramics, North Staffordshire Polytechnic, Stoke on Trent, ST4 2DE, UK.
§ *Previous address*: Thorn EMI Central Research Laboratories, Dawley Road, Hayes, Middlesex, the Mechanics Group, Department of Engineering, University of Reading. Now at Fison's Scientific Instruments, Manor Industrial Estate, Gatwick Road, Crawley, Surrey, UK.

0022–2461/91 $03.00 + .12

signatures when used in aeroengine casings. It also has a large potential impact on the mass marketing of domestic appliances if used, for instance, as lightweight oven casings and venturi, with simple one-piece units replacing the complex fabrications currently required to achieve the desired physical requirements.

In the composites discussed here the dimensions of the alumina and magnesia powder particles were 0.5 to 10 μm and 3 to 40 μm, whilst the milled fibres were short, 150 μm × 10 μm diameter. The prototype material suffers from serious void defects which can be several mm in diameter.

The purpose of the current research programme is to investigate the feasibility of non-destructively evaluating the structure of this and other ceramic materials by ultrasonic methods for quality control and process control applications. Measurement problems arose at low frequencies where the wavelength was greater than the sample dimensions and therefore one of the research objectives was to understand the nature of the wave propagation under such circumstances. This approach was taken in preference to preparing larger samples since in an industrial NDT application the ultrasonic technique must be tailored to the artifact to be examined and not the converse.

This communication is concerned with the frequency dependence of velocity at kHz frequencies, the reliable quantitative determination of grain size and elastic constants from attenuation and velocity data, and comparison of elastic data with theoretical expectations.

2. Preparation of samples

Aluminium orthophospate bonded alumina–magnesia ceramics, as described in previous reports [1, 2], were prepared with various chopped fibre contents.

When MgO powder reacts chemically with a solution of $Al(H_2PO_4)_3$ [3, 4], in the presence of Al_2O_3, a multiphase ceramic, consisting of several polycrystalline magnesium and aluminium phosphates with water of crystallization in specific crystalline planes, is produced. The reaction sequence is complex and the main reactions are essentially as follows.

Gibbsite and phosphoric acid react to produce aluminium orthophosphoric acid:

$$Al_2O_3 \cdot 3H_2O + 6(H_3PO_4) \approx 2Al(H_2PO_4)_3 + 6H_2O$$

Gibbsite — Phosphoric acid — Aluminium orthophosphoric acid

The aluminium orthophosphoric acid is allowed to retain water, and more is added, to produce a 48% by weight solution which reacts with magnesia in the presence of alumina thus

$$2MgO + Al(H_2PO_4)_3 \xrightarrow{H_2O} 2MgHPO_4 \cdot 3H_2O + AlPO_4 \cdot xH_2O$$

crystalline newberyite — amorphous

In the composites discussed here the dimensions of the alumina and magnesia powder particles were 0.5 to 10 μm and 3 to 40 μm, whilst the milled fibres were approximately 150 μm in length and 10 μm in diameter. The final phase assemblage for the reaction bonded material would be a matrix consisting ideally of about 70% crystalline newberyite, and 30% aluminium phosphate by weight with corresponding values of 79% and 21% by volume, assuming x to be 2. Whilst the prevalent reaction is as stated, others do occur leading to the formation of other magnesium phosphates, so that in practice small amounts of MgO, $(Mg(PO_3)_2$ and $MgH_2P_2O_7$ will be present. The filler, alumina and any fibre, 55 to 60% by weight, is dispersed throughout the matrix. In subsequent discussion the matrix should be understood to refer to all the reaction products whilst the particulate or fibrous fillers remain chemically inert although they may influence the end point of the matrix reactions and the amount of porosity in the matrix. Taking the alumina content to be 55% by weight there would be 31.3% newberyite and 13.5% aluminium phosphate by weight ignoring minor phases.

We shall consider three samples with starting compositions in wt % as in Table I. Test pieces of dimensions 1.5 × 1.5 × 6 cm^3 were produced using a co-rotary extruder as a compounding mixer. The mixture was extruded under vacuum, vibrated into moulds and set off at 100 or 20 °C.

3. Material structure

Simple observation of the surface shows that the prototype material suffers from serious void defects which can be several millimetres in diameter in extreme cases, and arise from gaseous reaction products and air incorporated during mixing and moulding. Hand lens observation of fracture surfaces reveals a coarse texture, with grain dimensions on a millimetre scale. Therefore another possible defect is poor intergranular bonding (which may be related to grain dimensions) due to departures from the intended chemical reaction route. This may stem from local variations in proportions and/or conditions. Such inhomogeneities are more likely with these multiphase composites than with simpler two-phase composites.

Samples were polished and examined under oblique illumination adjusted to give the greatest possible contrast between the two major phases observable. The photomicrographs are shown in Figs 1, 2 and 3. There are differences in the microstructures of the samples with grains of up to 2 mm in the 5% fibre samples (Fig. 1), grains up to 1 mm in the 1.5% fibre sample (Fig. 2), and grains up to 0.7 mm in the fibre-free samples. In all samples there are two main matrix phases visible, the softer phase containing the majority of the porosity. In the case of the no-fibre sample there is little contrast between the two matrix

TABLE I Starting compositions in wt %

Al_2O_3	55.5%	58.2%	57.92%	0%
$Al(H_2PO_4)_3$	33.43%	33.40%	33.80%	82.63%
in H_2O	48% solution	48% solution	60% solution	48% solution
MgO	6.07%	6.15%	8.28%	17.37%
Fibre	5.0% Glass	1.63% Carbon	Nil	Nil
Mean density ($kg\,m^{-3}$)	2356	2385	2326	1561
Setting temperature (°C)	100	100	20	20

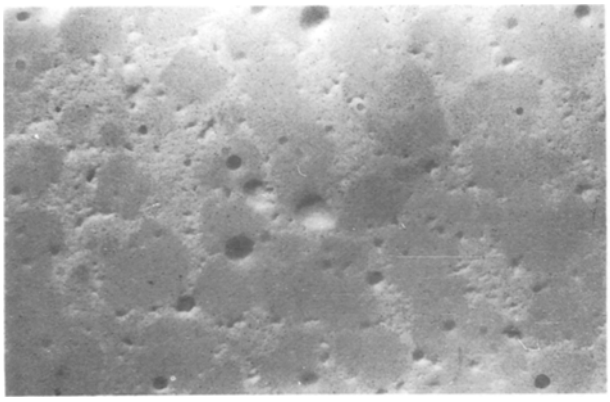

Figure 1 Photomicrograph of a polished section (over an area approximately $5 \times 3\ mm^2$) of the ceramic composite containing 5.0% glass fibre showing two-phase microstructure. Note the fibres in both main phases.

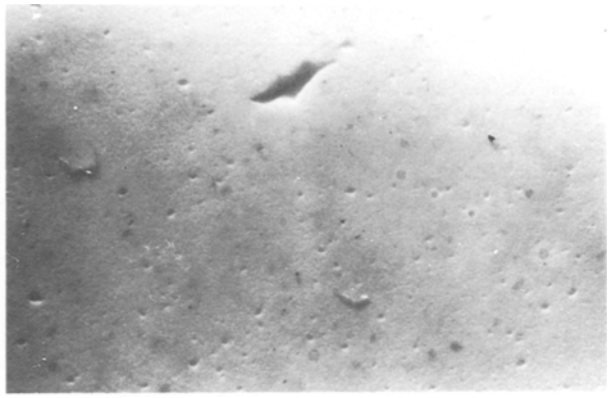

Figure 3 Photomicrograph of a polished section (over an area approximately $5 \times 3\ mm^2$) of the ceramic composite without fibre showing two-phase microstructure. Note the increase in porosity in various regions.

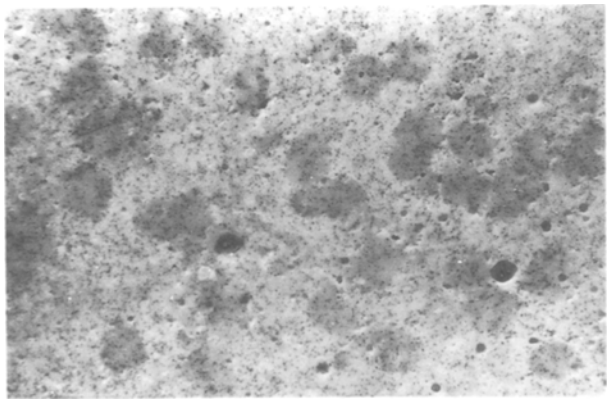

Figure 2 Photomicrograph of a polished section (over an area approximately $5 \times 3\ mm^2$) of the ceramic composite containing 1.5% carbon fibre showing two-phase microstructure. Note the fibres in both main phases.

phases, their presence being indicated by the arrangement of the pores.

In the case of the fibre-reinforced ceramics the individual fibres are visible in all phases and the differences in microstructure would not appear to be related to fibre content.

The overall structure of these materials can therefore best be described as a two-phase material, each phase being composed of a complex mixture of alumina, aluminium phosphate and newberyite, and the extent to which the proportions of these phases differ from the theoretical proportions described earlier is at present unknown.

4. Instrumentation

Time of flight velocity measurements were made with timing circuitry having a precision of 100 psec, over a range of frequencies from 24 kHz to 5 MHz, using a dual probe (pitch and catch) technique. It was found that this technique enabled propagation at higher frequencies than was possible when a single-probe pulse–echo technique was used, due to the reduction of path length by a factor of two, and the absence of noise due to backscatter from grain boundaries ever present in single probe techniques. The thickness was measured by means of a digital micrometer to an accuracy of 0.001 mm. Attenuation measurements spanning the continuous frequency range 250 kHz to 10 MHz were carried out using combined narrowband and broadband measurements.

4.1. Low frequency measurements 24 to 500 kHz

Measurements at 24, 37, 54, 82, 150, 220 and 500 kHz were made using the C.N.S. electronics PUNDIT (portable ultrasonic non-destructive digital indicating tester). This equipment uses two probes, one to transmit and the other to receive the ultrasonic pulse, and gives a digital readout of the transit time of the pulse through the sample. From these measurements and thickness data, measured by micrometer, the ultrasound velocity was calculated. The clock circuit measures the arrival time of the earliest negative going quarter cycle of the pulse to exceed the trigger threshold of 200 μV. If the sample attenuation is so high that

the threshold is not reached then no time measurement at all is obtained. Thus it appears that the fastest "observable" phase velocity in the received wave group is usually measured rather than a group velocity, which is the velocity with which the energy in a pulse of waves is transmitted [5]. By "observable" we mean, as implied earlier, that the waveform must exceed the trigger threshold, thus depending on attenuation levels and the spectral energy distribution in the pulse, the fastest observable phase velocity is not necessarily the fastest phase velocity in the wave components of the pulse.

Ultrasonic coupling between the probes and the sample was achieved using Castrol water pump grease. Whilst the grease is difficult to remove from the ceramic surface it has proved superior to an aqueous gel couplant (Krautmaker ultragel II) since this is absorbed by the porous ceramic leading to loss of adequate coupling and probably degradation of the ceramic in time. Care must be exercised when applying the grease since excessive amounts result in a thicker layer of couplant leading to low velocity values. Insufficient grease causes inadequate coupling which also leads to low values of sound velocity. Repeated use of grease for coupling sealed the ceramic surface to some extent and it was then possible to use ultragel II where prolonged coupling is not required.

4.2. High frequency velocity and narrow band attenuation measurements

Measurements of compressional wave velocities at frequencies of 1, 2.2 and 5 MHz, and shear wave velocities at a frequency of 5 MHz, were made using a Panametrics pulser-receiver PR 5052, linked to a digital delay generator accurate to $\pm$ 100 psec, in conjunction with a Tektronix 2445 dual trace 150 MHz oscilloscope, as shown in Fig. 4. This gives a waveform for the pulse on one channel, and a delayed marker pulse on the other channel. The delayed marker can be used to mark the position of each echo of interest on the oscilloscope screen, and the time difference between these echoes is thus obtained from the difference between the digital delay settings. For the greatest accuracy the oscilloscope is also triggered by the delay so that marking can be carried out using the fastest time base setting. This equipment can be used in single probe or dual probe configuration but for these samples the single probe technique was, in general, inadequate for frequencies above 2 MHz.

Narrow band attenuation measurements were made again using a dual probe technique and similar instrumentation. The pulser–receiver was linked via a high gain amplifier to the dual channel oscilloscope, the second channel of which was used as cursor. A switched attenuator, variable from 0 to 82.5 dB in 0.5 dB increments, was incorporated in the circuit.

Setting the sample between the probes, an optimal signal was obtained, the peak height being marked by the cursor trace. With all equipment settings remaining constant, a reference signal obtained with the probes in direct contact was reduced by the attenuator such that the peak height was the same as the sample peak height, as indicated by the cursor. This procedure was repeated for all three samples using probe frequencies of 0.25, 0.5, 1.25, 2.25, 5 and 10 MHz, several times in each case.

Some velocity and attenuation measurements were repeated using pulses of narrower band width from the Matec pulse modulator illustrated in Fig. 4. This data confirmed that errors in the original measurements with broader pulse bandwidths were negligible compared with other sources of experimental error.

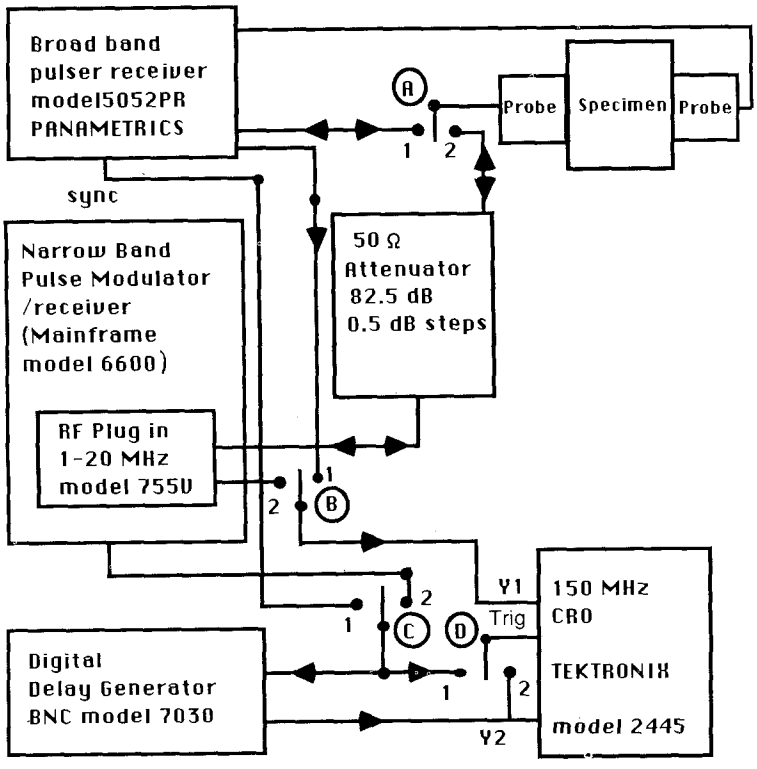

Figure 4 Instrumentation for ultrasonic velocity and attenuation measurements (attenuators are built into the Panametrics unit.). Switches A, B and C, are in position 1 for velocity measurements using fast rise time pulses, and in position 2 for higher precision velocity measurements using pulses of narrower frequency spectrum obtained by the use of a Matec pulse modulator (i.e. slow risetime and many cycles). Switch D is in position 1 for marking up pulses of interest and in position 2 to allow timebase expansion for precise time measurements. Matec units for automated attenuation measurements are omitted for clarity.

4.3. Spectrum analysis

Spectrum analysis was carried out using a Marconi Instruments spectrum analyser 2382 with display unit, together with a Panametrics pulser–receiver PR 5052, gated peak detector GPD 5052, and 5 MHz broad band probes, as shown in Fig. 5. Again a dual probe technique was used. The amplitudes may be in volts or dB with various standards. These can be subtracted and the difference displayed, thus giving a plot of frequency against attenuation in dB in the latter case.

The best results were obtained using a quartz disc as a buffer rod, taking as the reference the signal through the quartz, and subtracting from this the signal through the specimen and the quartz, to give a plot of attenuation against frequency. The buffer rod introduced the delay required to enable a correctly gated reference pulse to be obtained. The low level of attenuation introduced by the quartz, which was almost entirely due to diffraction effects rather than material absorption, was negated by the subtraction process. The grease proved to be the most suitable couplant being capable of maintaining constant bonds throughout the analysis process. Six repeat plots were made for every sample, each obtained with independent probe-sample bonds. These were superimposed on the same plot in different colours thus facilitating the reading of attenuation data for analysis.

5. Low frequency velocity measurements

In rods an infinite but discrete set of compressional wave modes (which we shall label by n, where $n = 1, 2, 3 \ldots$) are possible, each one having a dispersion relationship which depends on the dimensions of the sample perpendicular to the propagation direction (i.e. the rod axis). In each mode the pressure distribution across any section perpendicular to the rod axis is not uniform, thus to propagate a pure mode a non-uniform pressure distribution across the couplant-sample interface is required and it follows that a uniform pressure distribution in the couplant will necessarily lead to mixed mode propagation. This condition almost certainly applied in the present experiment because the transducers were too rigid to permit the formation of the meniscus-shaped coupling films required to produce non-uniform pressure distributions.

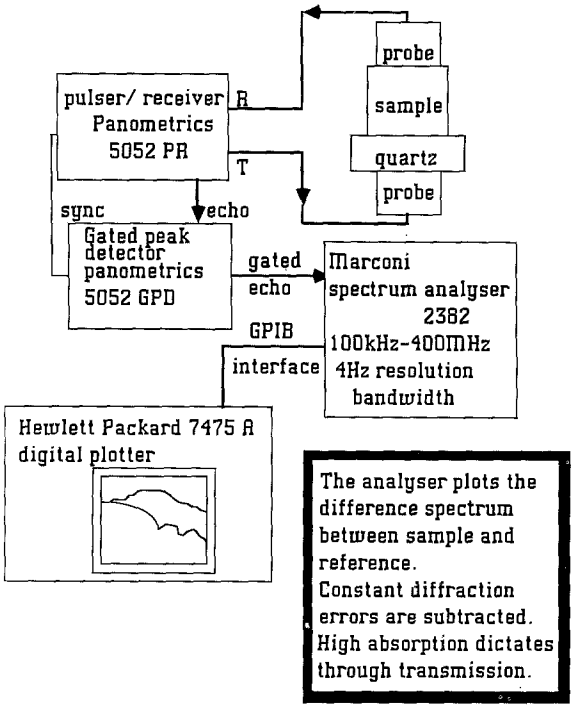

Figure 5 Instrumentation for the attenuation measurements made by means of spectrum analysis.

The above description describes qualitatively the solutions to the general wave equation subject to the boundary condition that the stress over the sidewalls of the rod must vanish. Quantitatively the solutions are exceedingly complicated. As a first approximation a simplified quantitative picture can be obtained as follows. Each mode consists of two compressional plane waves which travel back and forth across the sample at such an angle, α, that the boundary conditions can be satisfied. Divergence of the beam generated by the transmitting probe provides the necessary mechanism to launch the modes. It is obvious that an oblique motion of plane waves will lead to a non-uniform pressure distribution in cross-sections at right angles to the rod axis, although this distribution is only approximately similar to what is predicted from an exact solution of the wave equation. The non-uniform transverse pressure distribution and the zig-zag motion of plane waves both imply that there are transverse as well as axial components to the particle displacements, i.e. wave modes propagating axially in rods cannot be purely compressional i.e. exhibit axial motion only.

α is given by the equation

$$\cos\alpha = (j_0)_n c_L/a\omega \,. \tag{1}$$

where $(j_0)_n$ is the appropriate root of the bessel function j_0, c_L is the longitudinal wave velocity, and a is a term relating to the dimensions of the specimen.

This leads to a phase velocity along an axis given by

$$(c_p)_n = c_L/\sin(\alpha_L)_n = c_L/[1 - (j_0)_n{}^2 c_L/a^2\omega^2]^{0.5} \tag{2}$$

For a cylindrical rod a is the radius but for other geometries a is more complex. For a rectangular cross-section Kolsky [5] advocates

$$a = (d^2/3)^{0.5} \tag{3}$$

where d is the diagonal, as a dimensional term in a similar formula linking c_L and $(c_p)_n$.

It will be noted that there is a low frequency cut off point, ω_c, where $(c_p)_n$ rises asymptomatically to ∞ and below which no propagation is possible (imaginary $(c_p)_n$ values). Above the cut off $(c_p)_n$ decreases monotonically and asymptomatically to c_L as ω tends towards infinity. The finite frequency bandwidth of the pulses means that infinite phase velocities are not observable in practice. If the bandwidth of the pulse encompasses the cut-off frequency, because of the

asymptotic variation of $(c_p)_n$ close to the cut-off the proportion of the pulse energy content which travels at velocities approaching infinity is infinitesimal so that the leading cycles in the pulse are too small to be observed. In practice the velocity of a mode will be seen to rise to a high but finite value in the vicinity of the cut-off.

There is an additional longitudinal wave mode called the rod wave mode which has no low frequency cut-off but exhibits a maximum of

$$c_E(0) = (E/\rho)^{0.5} \quad (4)$$

where E is Young's modulus as ω tends towards 0. As ω increases $c_E(0)$ falls off continuously approaching the surface wave velocity as ω tends towards infinity. Now $c_E(0)$ is always less than c_L so that $c_E(0)$ is always less than $(c_p)_n$. Thus if a pulse consists of a mixture of the rod wave mode with one or more $(c_p)_n$ modes, the plot of the frequency dependence of the fastest observable phase velocity in the pulse will exhibit a maximum and limiting values of $c_E(0)$ and c_L as ω tends towards 0 and ∞, respectively. The maximum will lie somewhere within the range of cut-off frequencies for the different $(c_p)_n$ modes present. As ω drops below the cut-off point ω_c the velocity will not drop suddenly to c_E (which is $< c_L$). Instead, because of the finite bandwidth of the pulse extending to $\omega > \omega_c$ the velocity will fall off continuously from a maximum value, to $c_E(0)$ as ω tends towards 0.

Using the above model, typical cases of the theoretical frequency dependence are plotted in Figs 6a to 6c, for the fastest observable phase velocity (i.e. the speed of the first quarter cycle to be visible) of a longitudinal wave pulse. The three curves in each figure correspond to propagation consisting of the rod wave mode combined with the first, second and third $(c_p)_n$ modes, respectively. Velocities above the cut-off frequency are obtained from Equation 2 using the

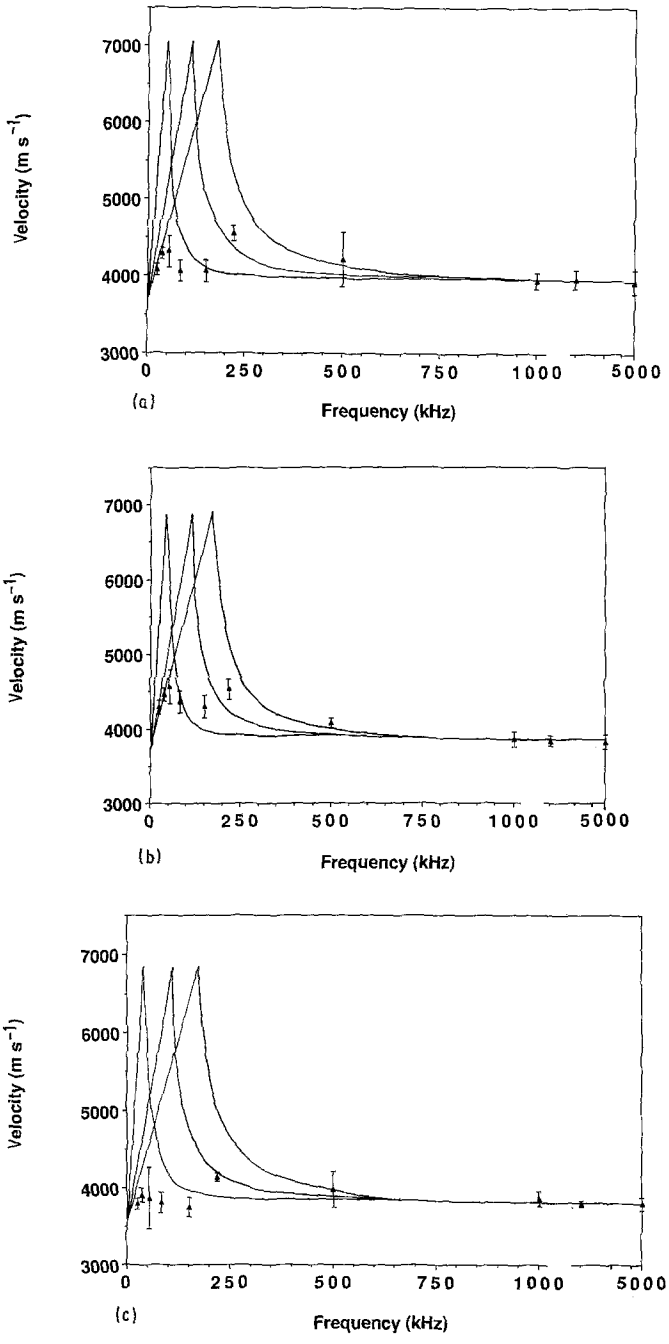

Figure 6 Actual and theoretical frequency dependence for the fastest observable phase velocity of a longitudinal wave pulse. The three curves correspond to propagation consisting of the rod wave mode combined with the first, second and third $(c_p)_n$ modes, respectively, obtained as described in the text from Equation 2 using the appropriate value of n, with a given by Equation 3 for a 1.5 × 6 cm^2 section, and c_L is taken as the compressional wave velocity measured at 5 MHz. (a) 5% glass fibre; (b) 1.5% carbon fibre; (c) no fibre content.

appropriate value of n, as given by Equation 3 for a 1.5 $\times$ 6 cm^2 section, and c_L being the experimental compressional wave velocity taken at 5 MHz.

At the cut-off frequency, ω_c, a finite value of c_n has been derived from the following argument. To a reasonable approximation a pulse of centre frequency ω has a spectrum bandwidth of $\omega \pm \omega_c/n$ where n is the number of cycles in the pulse, assumed of equal amplitude. Thus to a first approximation, because of finite bandwidth the velocity at the cut-off frequency, $c_n(\omega_c)$ may be taken as the velocity evaluated at the frequency $\omega_c + \omega_c/n$, i.e.

$$c_n(\omega_c) \approx c_L/[1 - 1/(1 + 1/n)^2]^{0.5} \quad (5)$$

Taking $n = 5$ as reasonable for the probes employed one obtains

$$c_n(\omega_c) \approx 1.8\, c_L \quad (6)$$

Finally velocities below the cut-off frequency are obtained by linear extrapolation between the value $c_n(\omega_c)$ from Equation 6, and c_E obtained from Equation 4 with E obtained from the compressional and shear wave velocities measured at 5 MHz (Table I), i.e. from c_L and c_T (Equations 1 and 2).

The experimental data points show presumed low frequency peaks of longitudinal wave velocity in the three samples in convincing agreement with the above model i.e. the data points lie within the bounds of the peak prescribed theoretically. Thus the results suggest that a mixture of $(c_p)_n$ modes of low n values (1, 2, 3) together with the rod wave mode were present at the lower frequencies. The measured velocity therefore is that of the fastest mode having a pulse amplitude in excess of the trigger threshold.

6. High frequency elastic moduli

It would now appear that at 220 kHz the peak in the velocity dispersion curve has been passed and above 2 MHz a steady velocity value independent of frequency obtains in a given sample of the size and shape considered here.

A comparison of ultrasonically measured elastic moduli with theoretical bounds for two-phase materials [9–11] can provide information about the material, given appropriate conditions. The experimental moduli and the volume fraction of the filler are obtained from the relationships

$$G = \rho c_T^2 \quad (7)$$

$$K = \rho c_L^2 - (4/3)G = \rho(3c_L^2 - 4c_T^2)/3 \quad (8)$$

$$E = 9KG/(3K + G) = \rho c_T^2(3c_L^2 - 4c_T^2)/(c_L^2 - c_T^2) \quad (9)$$

$$\sigma = (E/2G) - 1 = (c_L^2 - 2c_T^2)/2(c_L^2 - c_T^2) \quad (10)$$

$$V_2 = (\rho - \rho_1)/(\rho_2 - \rho_1) \quad (11)$$

where ρ is the mean sample density, c_L and c_T are the bulk and compressional wave velocities, respectively, K, G and E the bulk, shear and Young's moduli, respectively, σ the Poisson's ratio, V denotes volume fraction and the subscripts 1 and 2 denote matrix and filler properties, respectively.

The theoretical bounds of Hashin and Shtrikman denoted by H (upper bound) and L (lower bound), respectively, are, assuming that $K_2 > K_1$ and $G_2 > G_1$

$$K_H = K_2 + (1 - V_2)/[1/(K_1 - K_2) + 3V_2/(3K_2 + 4G_2)] \quad (12)$$

$$G_H = G_2 = (1 - V_2)/[1/(G_1 - G_2) + 6(K_2 + 2G_2)V_2/5G_2(3K_2 + 4G_2)] \quad (13)$$

$$K_L = K_1 + V_2/[1/(K_2 - K_1) + 3(1 - V_2)/(3K_1 + 4G_1)] \quad (14)$$

$$G_L = G_1 + V_2/[1/(G_2 - G_1) + 6(K_1 + 2G_1)(1 - V_2)/5G_1(3K_1 + 4G_1)] \quad (15)$$

By combining Equations 7 to 11 with Equations 12 to 15 corresponding bounds on all the other moduli and Poisson's ratio can be calculated if required.

The Hashin and Shtrikman bounds are valid for arbitrary phase geometry (i.e. any particle size and shape distribution and any spatial distribution of particles) providing that certain conditions hold. These are (i) the particle dimensions are small with respect to $\lambda/4$, (ii) adhesion between the filler and the matrix is good, and (iii) there are no voids in the matrix. If an additional condition holds, namely that the particles are spherical, then the experimental data should lie exactly on the lower bound.

It is clear that the types of defects likely in this material may be signalled by the departure of experimental moduli from the Hashin and Shtrikman bounds. For example, sufficiently poor filler matrix adhesion may cause ultrasound to propagate only in the matrix so that the experimental moduli lie much lower than the lower bound. Voids produce a similar effect by lengthening the effective path length of ultrasound in the matrix. Agglomeration will cause the experimental moduli to be frequency dependent [9] if the size of the agglomerates become comparable with or larger than 0.25 of a wavelength. Since, for typical high modulus fillers, the Hashin and Shtrikman bounds will be quite broad, the technique will work best when spherical particles are present so that only the lower bound need be considered as a quality indicator for the sample.

The elastic contents determined using Equations 7 to 10 are given in Table II. The most striking feature of these results is that the bulk modulus of the fibre-free ceramic is a factor of 10 less than the bulk moduli of the constituent oxides, magnesia and alumina, which are 162 and 252 GPa, respectively. When such a large change of modulus occurs during a manufacturing process there are obvious prospects of using this property for non-destructive process monitoring, since only a slight departure of the final material from its intended composition may produce substantial modulus variations. It is interesting to note that the elastic moduli of the three finished samples differ by less than 10%, notwithstanding the order of magnitude change in modulus during processing mentioned previously.

TABLE II Elastic constants measured at 5 MHz

	5% Glass	1.5% Carbon	no fibre	no alumina
Shear modulus (GPa)	14.33	14.77	12.66	2.30
Bulk modulus (GPa)	17.33	15.12	16.67	5.20
Young's modulus (GPa)	33.70	33.42	30.30	6.01
Poisson's ratio	0.18	0.13	0.19	0.30

It seems reasonable, therefore, to assume that the final modulus achieved is the norm to be expected when the chemical reactions proceed as intended (we have assumed in this argument that the contribution of the fibres to the modulus at MHz frequencies is small due to the low filler volume fraction).

As will subsequently become apparent, the reason why the modulus of the final product is so much less than that of the starting oxides is not the presence of the weak hydrogen bonding in the waters of crystallization. The magnesium and aluminium phosphate structures in the matrix consist of three-dimensional networks of closed rings of strong metal (aluminium, magnesium and phosphorus)–oxygen bonds (Figs 7 and 8). These rings, and not the hydrogen bonding, govern the elastic constants. These rings have diameters almost twice as large as those occurring in the starting oxides, and assuming an approximate inverse fourth power law relationship [12] between ring diameter and bulk modulus, we should not be surprised to find moduli values in the final product up to 16 times smaller than values obtaining in alumina and magnesia. Further reductions in the final modulus would be caused if free water (rather than just bound water) were still present because the former would constitute an additional phase of very low modulus.

A sample of material with the same aluminium acid phosphate:magnesia ratio but devoid of alumina or fibre fillers was prepared. This was found to have a density of 1561 $kg\,m^{-3}$, and elastic constants as given in Table II. Substituting this density and those of an alumina filled but fibre-free sample, and alumina, 2356 and 3980 [4], respectively, into Equation 11 a matrix volume fraction of 0.67 is obtained. This is in good agreement with the matrix volume fraction of 0.70 obtained from consideration of the starting composition, and implies that the alumina is simply a space filler and takes little part in the reaction. It would, therefore, seem reasonable to assume that the elastic constants of the matrix in the alumina-filled composite are very similar to those obtained for this unfilled sample.

Proceeding on this assumption Hashin and Shtrikman bounds for an alumina filled but fibre-free sample were calculated considering the matrix (unfilled) material and alumina as the end members such that

$$K_1 = 5.2 \quad K_2 = 251.2 \quad G_1 = 2.3$$

$$G_2 = 163.4 \quad V_1 = 0.67 \quad V_2 = 0.33$$

Substituting in Equations 12 to 15 for an alumina filled but fibre-free sample we obtain bounds for bulk modulus of 9.32 and 52.09 GPa, and for shear modulus of 4.42 and 34.75 GPa. The actual measured values

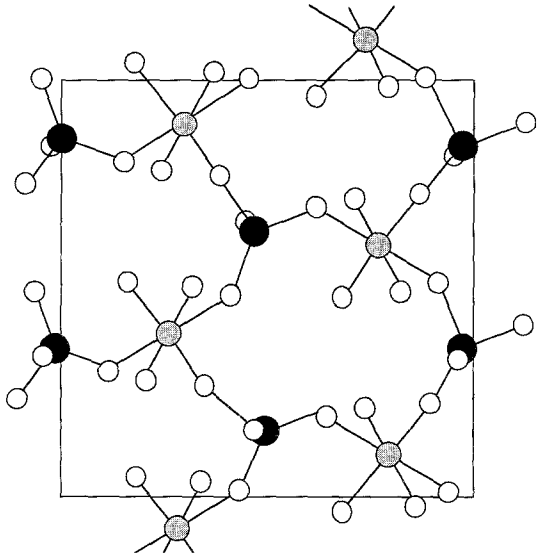

Figure 7 Unit cell structure of crystalline newberyite after Sutor [11]. The magnesium atoms are approximately coplanar and lie between two planes of phosphorous atoms. They are coordinated octahedrally by the oxygen atoms from the phosphate groups and the three water molecules. The hydrogen atoms have been omitted for clarity. (○ Mg, ● P, ○ O)

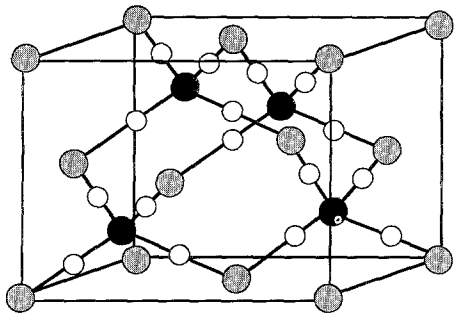

Figure 8 Unit cell of anhydrous aluminium orthophosphate. The coordinations of Al (●) and P (○) with oxygen are identical but for clarity, two bonds between each P and O (○) have been omitted.

(column 3, Table II) lie between these two bounds towards the lower bound and thus one can conclude that there is no definite layer structure, nor are the particles spherical since the moduli are not at the lower bound. It would be reasonable to assume, therefore, that the particles are flattened or plate like. This assumption has since been confirmed by scanning electron microscopy [13].

The structure of newberyite, an end product of the reaction, was documented by Sutor [14] who worked on crystalline material from Skipton Caves, Australia. The structure is illustrated in Fig. 7 after Sutor. Using

this structural data, a theoretical value for the bulk modulus was calculated using the model of Bridge and Higazy [10] from the relationship

$$K = S\sum_{i=1}^{n}(n_f)_i(N_f)_i r_i^2 F_i \qquad (16)$$

where for bond type i, $(N_f)_i$ is the number of formula units in which the bond resides per unit volume, $(n_f)_i$ is the number of network bonds per formula unit, r_i is the network bond length, and F_i is the first-order stretching force constant. The factor S is < 1 and decreases with the extent to which isotropic elastic deformation leads to bending rather than direct compression of bonds [12]. The summation function, conveniently abbreviated to K_{bc}, represents the bulk modulus that would obtain if no bond bending takes place. Values of F_i can be estimated from the empirical relation

$$F = 5.28N\frac{(X_a X_b)^{3/4}}{r^2} = 30\,\mathrm{N\,m^{-1}} \qquad (17)$$

where r is in nm, N is the bond order, and X_a and X_b are the electronegativities of the two atoms.

Denoting $i = 1$ and 2 for Mg–O and P–O bonds, respectively, and neglecting the much weaker H–O–H bonds the following list of values can be drawn up, the values for r being the mean of the reported values,

1 Mg–O $(nf)_1 = 3$ $r_1 = 0.2039$ nm

$F_1 = 198\,\mathrm{N\,m^{-1}}$

2 P–O $(nf)_2 = 3$ $r_2 = 0.1529$ nm

$F_2 = 424\,\mathrm{N\,m^{-1}}$

where the simplest formula unit as obtained from Fig. 7 has been employed and F values have been obtained from Equation 17 by the use of electronegativity values (Alfred–Rochow scale) [15] of 1.2, 2.1 and 3.50 for magnesium, phosphorus and oxygen, respectively. We also have in this case

$$(N_f)_1 = (N_f)_2 = N_A\rho/M \qquad (18)$$

where N_A is Avogadro's number, ρ is the density, and M is the molecular weight of newberyite.

The theoretical value of density reported by Sutor is $2119\,\mathrm{kg\,m^{-3}}$ so that $N_f = 7.32 \times 10^{27}\,\mathrm{m^{-3}}$. Substituting this and the other data above into Equation 16, we obtain

$$K_{bc} = 44.31\,\mathrm{GPa} \quad \text{(for a single crystal)}$$

A value for S can be arrived at by the use of Fig. 9 [11, 14] which presents a systematic relationship between atomic ring size (i.e. the shortest closed circuit of bonds) and K_{bc}/K_e (where K_e is the experimental modulus) for simple oxide structures. The smallest mean ring diameter (circumference/π) in the unit cell of newberyite is 0.68 nm, so that from Fig. 8 $S \approx 0.2$ and

$$K = 0.2K_{bc} = 8.86\,\mathrm{GPa}$$

The other end member of the reaction, aluminium phosphate can crystallize in several forms, some with various degrees of hydration. The anhydrous form

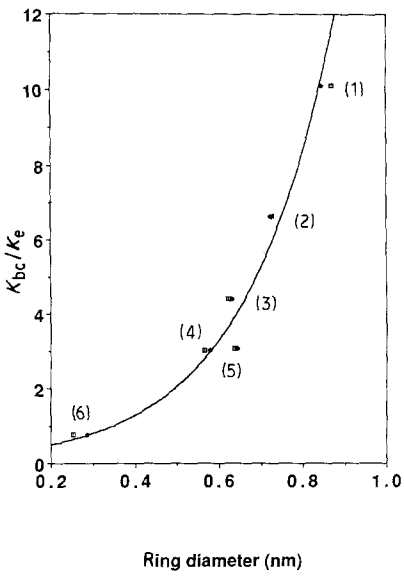

Figure 9 Dependence of K_{bc}/K_e on the mean atomic ring size in pure oxide glasses, where K_{bc} is the theoretical bulk modulus that would arise if bonds did not bend during isotropic deformation, and K_e is the experimental modulus. The numerals denote materials as follows: 1 B_2O_3, 2 AS_2O_3, 3 GeO_2, 4 SiO_2, 5 P_2O_5, 6 Diamond. Scatter of data points derive from two independent methods of ring size calculation (see [12]).

stable at ambient temperatures is berlinite which has the structure illustrated in Fig. 8 [4, 16] and a density of $2566\,\mathrm{kg\,m^{-3}}$ [17]. The aluminium and phosphorous have, respectively, electronegativities of 1.5 and 2.1, bond lengths with oxygen of 0.170 and 0.156 nm [14, 16], and coordination number of 4. Thus from equations 17 and 18 and taking the simplest possible formula unit from Fig. 8 we derive the following values

1 Al–O $(nf)_1 = 4$ $r_1 = 0.170$ nm

$F_1 = 291\,\mathrm{N\,m^{-1}}$

2 P–O $(nf)_2 = 4$ $r_2 = 0.156$ nm

$F_2 = 413\,\mathrm{N\,m^{-1}}$

Substituting the data above into Equation 16 and taking $(N_f)_2$ to be $1.26 \times 10^{28}\,\mathrm{m^{-3}}$ we obtain

$$K_{bc} = 93.6\,\mathrm{GPa} \quad \text{(for a single crystal)}$$

The mean atomic ring size of 0.622 nm gives from Fig. 9 a value for S of 0.29 and

$$K = 0.29\,K_{bc} = 27\,\mathrm{GPa}$$

Given the reaction equation proposed in this paper the volume fraction of newberyite in an unfilled ceramic is about 80%. Thus given the theoretical estimates for the bulk moduli of newberyite and aluminium orthophosphate, 8.9 and 27 GPa, respectively, we can apply the Hashin and Shtrikman formulae (Equations 12 and 14) to compute theoretical bounds on the bulk modulus of the unfilled ceramic product. Since our theory does not include a computation of shear moduli for newberyite or aluminium orthophosphate we make the approximation that G_1 and G_2 in Equations 12 and 14 are equal to the experimental shear modulus of the ceramic product,

2.30 GPa. The result is

$K = 10.4$ GPa (theoretical estimate for non-porous unfilled ceramic)

there being no difference between the upper and lower bound within the first three significant figures. If we had used the broader Voigt and Reuss theoretical bounds which do not require a knowledge of end-member shear moduli, the resultant predicted bounds on K would have still been quite narrow, 10 and 12.5 GPa.

So far we have only considered ideal pore-free samples. Substitution of the theoretical (unit cell) density of newberyite (2111 kg m^{-3}) and aluminium orthophosphate (2566 kg m^{-3}) into Equation 11, with the assumed volume fraction of newberyite being 0.8, the theoretical density of the non-porous product is 2208 kg m^{-3}. The density of the actual product was, however, 1561 kg m^{-3}. Substitution of these two densities in Equation 11 and taking the density of the pores to be zero, shows that the volume fraction of porous voids was 0.293. If pores are assumed spherical and much smaller in diameter than the ultrasonic wavelength, then the elastic moduli of the porous material are given by [18]

$$K = K_0(1 - V)/(1 + f_1 V) \quad (19)$$

$$G = G_0(1 - V)/(1 + f_2 V) \quad (20)$$

where

$$f_1 = (1 + \sigma_0)/2(1 - 2\sigma_0) \quad (21)$$

$$f_2 = (4 - 5\sigma_0)/2(7 - 5\sigma_0) \quad (22)$$

V denotes the porosity (volume fraction of pores), and the subscripted K, G and σ values denote values for the ideal pore-free material, i.e. the matrix.

We have no theoretical estimate for σ, however since f_1 varies slowly with realistic values of σ_0 we will take for this quantity the measured Poisson's ratio for the unfilled ceramic, 0.30 (Table II, column 4). Taking $V = 0.29$, and $K_0 = 10.4$, (our theoretical value for the ideal ceramic), substitution in Equations 19 and 21 gives

$K = 5.0$ GPa (theoretical estimate for actual unfilled ceramic)

in remarkable agreement with the experimental value of 5.20 (Table II, column 4). This result gives complete support to our hypothesis that newberyite is the main reaction product.

In the above theoretical model of the elastic behaviour of the ceramic matrix, starting with Equation 16, we have made an implicit assumption that the presence of hydration does not affect moduli values dramatically. This seems a reasonable assumption when one considers that in both the newberyite and aluminium orthophosphate structures there are closed ring networks comprising Al–O, Mg–O and P–O bonds so that there is no question of weak hydrogen bonds breaking open what are essentially three-dimensional networks of strong and relatively directional bonds. If such an effect had been present the K_{bc}/K_e-ring size relationship employed (Fig. 8) would have been invalid.

The excellent agreement between theory and experiment achieved in the above analysis provides an example of how ultrasound velocity (moduli) measurements can be used for quality control and assurance purposes. Comparison between experimental data and theoretical data may allow one to decide non-destructively i.e. without sectioning or chemical analysis whether the final reaction products are as intended or whether the level of porosity in the matrix is within tolerable limits. Additionally, ultrasonic monitoring in the early stages of curing, with feedback to the production line may well prove to be an effective method of process control, leading to an optimum material structure and components of consistent high quality. A considerable research effort on the non-destructive monitoring of the curing process has been undertaken, and two of the authors have been involved in the publication of the findings elsewhere [19, 20].

7. Attenuation data

The attenuation data obtained by narrow band and spectrum analysis techniques are shown in Figs 10 and 11. The spectrum displayed on the VDU could also be printed on a digital plotter via the GPIB interface of the analyser, which can also display and plot the difference between any two spectra of interest. Difference spectra between samples and a quartz buffer rod reference were plotted. Six repeat plots were made for every sample, each obtained with independent probe-sample bonds, and from these the data and error bars for Fig. 11 were derived. Plots for the three samples under discussion are given in Figs 12, 13 and 14. The attenuation data show considerable differences in the frequency dependence of the three samples indicating a considerable potential of the measurements for materials sorting.

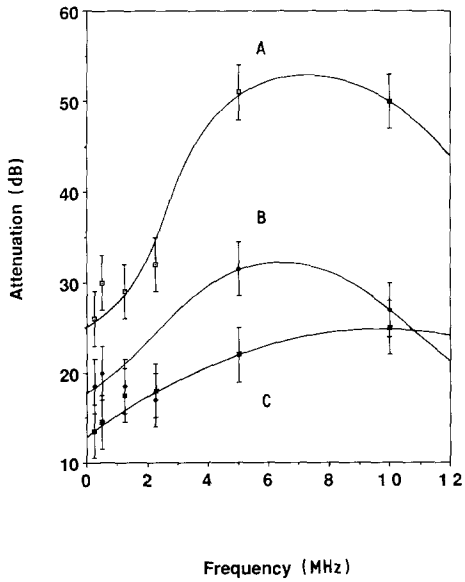

Figure 10 Plot of attenuation against frequency determined by the narrowband technique on 1.5 cm ceramic blocks with various fibre contents: A, 5% glass fibre; B, 1.5% carbon fibre; C, no fibre content.

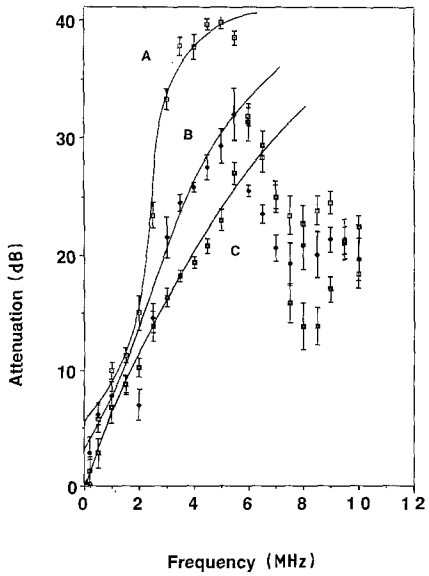

Figure 11 Plot of attenuation against frequency determined by spectrum analysis using 5 MHz probes on 1.5 cm ceramic blocks with various fibre contents: A, 5% glass fibre; B, 1.5% carbon fibre, C, no fibre content. Error bars are derived from the six independent spectrum plots in each of Figs 12 to 14.

Examination of the frequency regime in which the data are the most reliable (2 to 4 MHz) establishes that the attenuation of all samples varies as the first power of the frequency. This may be due in part to a hysteresis or multirelaxational loss, but if there is a scattering contribution (α_s) it must be of the stochastic type, i.e. $\lambda/3 < d < 3\lambda$ and $\alpha_s \approx \text{const}_2 \cdot df$. Given the typical wave velocity of 4000 m sec^{-1}, λ lies in the range 1 to 2 mm, implying extreme bounds of 0.3 to 6.0 mm for d. Thus scattering from fibres cannot account for the observed frequency dependence since the geometrical mean of their cross-section is only 0.04 mm, which satisfies the condition $d \ll \lambda$ and would imply a d^3f^4 term in the attenuation coefficient i.e. Rayleigh scattering. Thus grain boundaries must be the dominant scatterer in the frequency regime under discussion. For the glass fibre filled sample the attenuation became frequency independent above about 6 MHz, implying that diffusive scattering conditions have begun to hold, that is $d > 3\lambda$ and $\alpha_s \approx \text{const}_2 \cdot /d$. Since λ is 0.6 mm at 6 MHz then one can estimate the scattering particles to have dimen-

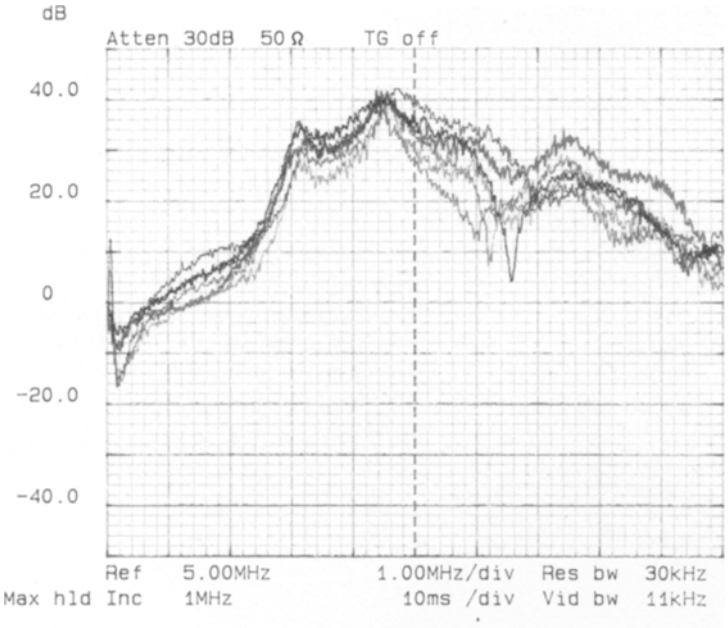

Figure 12 Difference spectra between ultrasonic pulse amplitude through 1.5 cm thick ceramic samples and a quartz buffer rod reference as plotted by digital plotter for ceramic composite containing 5% glass fibre.

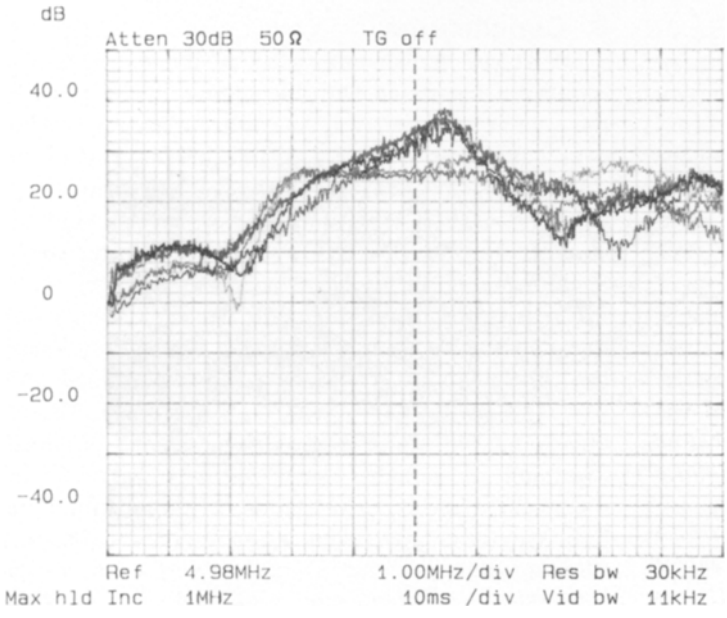

Figure 13 Difference spectra between ultrasonic pulse amplitude transmitted through 1.5 cm thick ceramic samples and a quartz buffer rod reference as plotted by digital plotter for ceramic composite containing 1.5% carbon fibre.

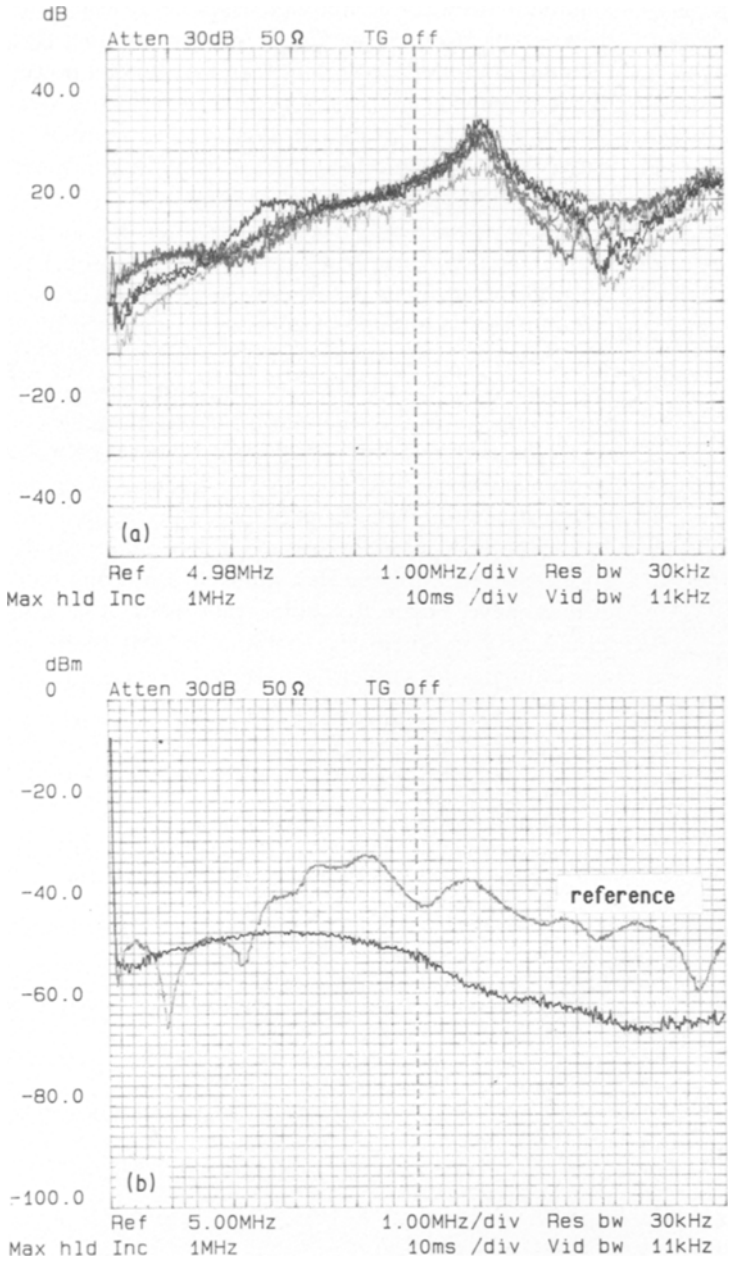

Figure 14 (a) Difference spectra between ultrasonic pulse amplitude transmitted through 1.5 cm thick ceramic samples and a quartz buffer rod reference as plotted by digital plotter for ceramic composite containing no fibre. (b) An example of actual sample and quartz reference spectrum and a quartz reference sample from which difference spectra (ie. sample spectra) were derived.

sions of 1.8 mm. Then taking attenuation data at 3 MHz and ignoring the possible presence of an absorption contribution to the attenuation one can estimate the dimensions of the scatterers in the other samples which do not exhibit a plateau in the attenuation against frequency plots. The result is $d = 1.2$ mm and 0.5 mm for the carbon fibre filled sample and the non-fibre sample respectively. The above three estimates are in rather good agreement with the results of microscopy on polished specimens, (see Section 3, Figs 1, 2 and 3).

At frequencies higher than those presently investigated the Rayleigh scattering contribution from the filler particles would begin to become relatively strong compared with the diffusive scattering from grains, and the multirelaxational and/or hysteresis losses. However the high level of these "background" losses will require thinner samples or increased probe output power for filler scattering to be detectable.

8. Conclusions

(1) At low frequencies, such that the wavelength is significant compared with the sample size, a peak in the velocity–frequency dispersion curve arises. This peak has been shown to be explicable in terms of the simultaneous propagation of the rod wave mode and first one or two longitudinal wave modes, and an assumption that the pulse bandwidths are about $\pm$ 10%.

(2) In materials of reasonable density the high frequency shear and compressional velocities, and hence the elastic moduli, could be easily determined and would be useful for QA and NDE purposes. Alternatively an indication of density could be obtained assuming a standard value of modulus for the specimen. Inability to propagate a certain minimum frequency could be taken as an indication of substandard material.

(3) The low frequency peak velocity position

appears to be highly sensitive to material property variations and therefore suitable for NDE purposes. Unfortunately this is extremely difficult to determine practically and interpret theoretically. On line computers and probe development could perhaps in the long term facilitate the application of these techniques.

(4) It is possible to differentiate between the three samples examined by observation of their frequency spectra. The extent of the ability of this technique to characterize specimens has yet to be determined. It should be possible to identify poor material by changes in the spectrum, and it may be possible to differentiate between batches of similar material in a quality assurance situation, dependent upon the extent of the material property variation.

(5) It is possible to determine the attenuation frequency relationship and from this to estimate the grain size of the material assuming grain boundary scattering. Since the grain size is dependent upon the production process and chemical reaction, and may even be indicative of the end point of the reaction, spectrum analyser plots and attenuation-frequency curves could prove invaluable in process monitoring and quality control of the material.

(6) In all samples there are two main matrix phases visible, on microscopic examination, the softer phase containing the majority of the porosity. Precise compositions and structures of these two phases are not yet available from X-ray diffraction studies, hence it is not at this point possible to determine Hashin and Shtrikman upper and lower bounds based on these phases. However, a theoretical calculation of bulk modulus based on the assumption that the matrix consisted of 80% newberyite and 20% aluminium orthophosphate by volume, was in excellent agreement with the measured matrix modulus after allowing for porosity. Such comparisons highlight the potential value of ultrasound velocity (moduli) measurements for non-destructive evaluation and quality control of this ceramic material.

Acknowledgements

The financial support of SERC and Thorn EMI is acknowledged under a project entitled "Non-Destructive Evaluation of Novel Materials", SERC 865D05. The work described in this paper was commenced at Brunel University and completed at the South Bank Polytechnic, London.

References

1. R. ROUND, B. BRIDGE and A. GREEN, *J. Mater. Sci. Lett.* **7** (1988) 305.
2. *Idem., ibid.* **7** (1988) 748.
3. J. E. CASSIDY, "High Temperature Chemistry of Inorganic and Ceramic Materials", edited by F. P. Glasser and P. E. Potter (Chemical Society, London, 1977) pp. 192–203.
4. W. D. KINGERY, *J. Amer. Ceram. Soc.* **33** (1950) 239.
5. H. KOLSKY, "Stress Waves in Solids" (Dover Books, New York, 1963) Ch. 3.
6. H. LAMB, *Proc. R. Soc. A*, **93** (1917) 114.
7. A. A. HIGAZY, PhD Thesis, Brunel University (1984).
8. R. W. MORSE, *J. Acoust. Soc. Amer.* **20** (1948) 833, **22** (1950) 219.
9. B. BRIDGE and K. H. CHENG, *J. Mater. Sci.* **22** (1987) 3118.
10. B. BRIDGE and A. A. HIGAZY, *Phys. Chem. Glasses* **27** (1986) 1.
11. B. BRIDGE and R. ROUND, *J. Mater. Sci. Lett.* **7** (1988) 63.
12. B. BRIDGE, N. D. PATEL and D. N. WATERS, *Phys. Status Solidi a*, **77** (1983) 655.
13. L. L. MATURANA, J. MSc dissertation, Brunel University (1988).
14. D. J. SUTOR, *Acta Crystallogr.* **23** (1967) 418.
15. F. A. COTTON and G. WILKINSON, "Advanced Inorganic Chemistry" 3rd Edn (Interscience Publishers, London, 1972) p. 115, Table 3–3.
16. R. W. G. WYCOFF, "Crystal Structures", Vol. 3, 2nd Edn (Interscience Publishers, London, 1965).
17. "C.R.C. Handbook of Chemistry and Physics", 65th Edn edited by R. C. Weast (CRC Press, Boca Raton, Florida, 1984) p. B69.
18. W. KREHER, J. RANACHOWSKI and F. REYMUND, *Ultrasonics* **15** (1977) 70.
19. K. S. TAN, R. ROUND and B. BRIDGE, *Brit. Ceram. Trans. J.* **88** (1989) 138.
20. T. KATHRINA, R. ROUND and B. BRIDGE, *J. Phys. D.* forthcoming.

Received 27 November
and accepted 6 December 1989